Multiplexed Long-Range Electrohydrodynamic Transport and Nano-Optical Trapping with Cascaded Bowtie Photonic Crystal Nanobeams

Sen Yang[1,3,*], Joshua A. Allen[1,3,*], Chuchuan Hong[2,3], Kellen P. Arnold[1,3]
Sharon M. Weiss[2,1,3] and Justus C. Ndukaife[2,1,3,†]

[1]*Interdisciplinary Materials Science, Vanderbilt University, Nashville, Tennessee 37235, USA*
[2]*Department of Electrical and Computer Engineering, Vanderbilt University, Nashville, Tennessee 37235, USA*
[3]*Vanderbilt Institute of Nanoscale Science and Engineering, Vanderbilt University, Nashville, Tennessee 37235, USA*

Photonic crystal cavities with bowtie defects that combine ultrahigh Q and ultralow mode volume are theoretically studied for low-power nanoscale optical trapping. By harnessing the localized heating of the water layer near the bowtie region, combined with an applied alternating current electric field, this system provides long-range electrohydrodynamic transport of particles with average radial velocities of 30 μm/s towards the bowtie region on demand by switching the input wavelength. Once transported to a given bowtie region, synergistic interaction of optical gradient and attractive negative thermophoretic forces stably trap a 10 nm quantum dot in a potential well with a depth of 10 $k_B T$ using a mW input power.

On-chip nanophotonic devices have been extensively studied in the past years based on their capability to concentrate and manipulate light [1–4]. Among them, nanoscale optofluidic chips incorporating plasmonic and photonic crystal cavities have recently emerged as a powerful platform for chemical and biological sensing [5], nanomanipulation [6] and optical nano-assembly [7,8]. Owning to the nanoscale feature of the cavities, the directed transport of nanoparticles and biomolecules to the region of highest electromagnetic field enhancement is critical to device performance. Though plasmonic nanocavities can support localized electromagnetic hotspots, they suffer from intrinsic material loss that gives rise to low quality factor (Q factor) resonances with broad spectral linewidths. This makes realizing multiresonant plasmonic cavities for wavelength switchable trapping and long-range particle transport extremely challenging. Dielectric photonic crystal (PhC) cavities, on the other hand confine light by means of a defect in an otherwise periodic arrangement of high index dielectric photonic structures [9,10] leading to low-loss, narrow linewidth resonances that can be leveraged for wavelength switchable trapping applications. To date, the deterministic transport of particles for interaction with the enhanced field near resonant PhC cavities has been met with challenges. Prior reported attempts to achieve transport of particles to PhC cavities rely on pressure-driven flow [11,12]. Unfortunately, this has limited particle capture rate because only the particles in the fluid boundary layer near the cavity can interact with the electromagnetic hotspots. Additionally, such pressure driven flow does not provide the mechanism for actively transporting particles from one nanocavity to the next.

In this Letter, we investigate the physics of light-induced near-field trapping, attractive negative thermophoresis, and long-range electrohydrodynamic transport of nanoparticles in bowtie PhC cavities for directional delivery of particles and trapping at the cavity region by switching the input wavelength. We note that the earlier work theoretically demonstrating the single nanoparticle trapping capabilities of such PhC structure [13] only considered the optical trapping alone, while other thermal-induced effects such as the wavelength-actuated electrothermal flow was not included. An important distinction between this Letter and our earlier work with plasmonic tweezers [14] is that the bowtie PhC is effectively lossless so that the electrothermal flow is induced by the enhanced absorption of the water medium layer by the localized and enhanced electric field of the bowtie PhC. In plasmonic tweezers, the plasmonic material is the lossy media. Accordingly, the use of the bowtie PhCs enables both low-loss nanophotonic tweezers and rapid particle transport on-demand. Furthermore, this Letter describes the actuation of electrothermal flow by means of switching the wavelength of light coupled to the cascaded PhC cavities for the first time. This is only possible in high-Q PhC cavities because of the high-Q and the ability to couple light in-plane. Such multiwavelength actuation of electrothermal flow is not possible in plasmonic structures which are characterized with large linewidths.

As shown in Fig. 1, a PhC nanobeam with a bowtie defect at the center is placed beside a bus waveguide to enable evanescent coupling from the side. For multiplexed long-range nanoparticle transport and trapping across cavities, we design the system to contain ($n = 3$) engineered bowtie PhC nanobeams (BPCNs) cascaded along the bus waveguide, each having a specific resonance wavelength. Light is coupled into the device through the
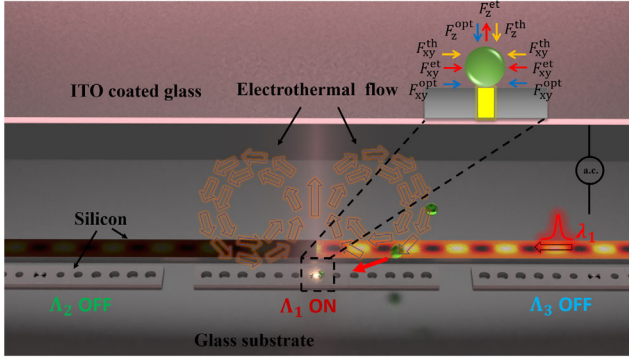
FIG. 1. Schematic of the PhC-based multiplexed long-range electrohydrodynamic transport and trapping system. The inset shows the forces experienced by a particle trapped at the bowtie. Optical force (opt), electrothermal force (et), and thermophoretic force (th).

bus waveguide and then extremely localized in the bowtie defect. The figure illustrates that a fundamental TE mode with the wavelength of λ_1 is propagating in the bus waveguide and coupled to the middle BPCN (Λ_1), inducing the cavity resonance, and switching the cavity to the "ON" state. With a bus waveguide width of 480 nm and coupling gap of 150 nm, the loaded Q of the side-coupled BPCN is 1.5×10^4 and the coupling efficiency [15] is 62% in a water environment. The peak electric field amplitude is 138 times higher in the bowtie compared to that of the light input into the bus waveguide, resulting in an electromagnetic field intensity enhancement of ~19 000. For details about the design of the BPCNs, please see Supplemental Material S1 [16]. The electric field profile of the side-coupled BPCN is shown in Fig. 2(a), where the extreme light localization at the center of the bowtie can be easily observed. To obtain different resonance wavelengths for the other two BPCNs, we slightly adjust the period of the PhC holes by −4 and +4 nm, respectively. Figure 2(b) shows the transmission spectra presenting the multiresonant property of our system.

Next, we characterize the optical trapping performance of the optimized BPCN system. An enhanced optical gradient trapping force requires a spatially confined electromagnetic field, which is provided by the bowtie gap. The time averaged optical force exerted on a nanoscale object is calculated by integrating the Maxwell's stress tensor (MST) [48] over an arbitrary surface enclosing the nanoscale object, which is given by

$$\langle \mathbf{F} \rangle = \oint_S \langle \overleftrightarrow{\mathbf{T}} \rangle \cdot d\mathbf{S}, \tag{1}$$

where $\langle \overleftrightarrow{\mathbf{T}} \rangle$ is the time averaged Maxwell's stress tensor given by

$$\langle \overleftrightarrow{\mathbf{T}} \rangle = \frac{1}{2} \mathrm{Re} \left[\varepsilon \mathbf{E} \mathbf{E}^* + \mu \mathbf{H} \mathbf{H}^* - \frac{1}{2} (\varepsilon |\mathbf{E}|^2 + \mu |\mathbf{H}|^2) I \right]. \tag{2}$$
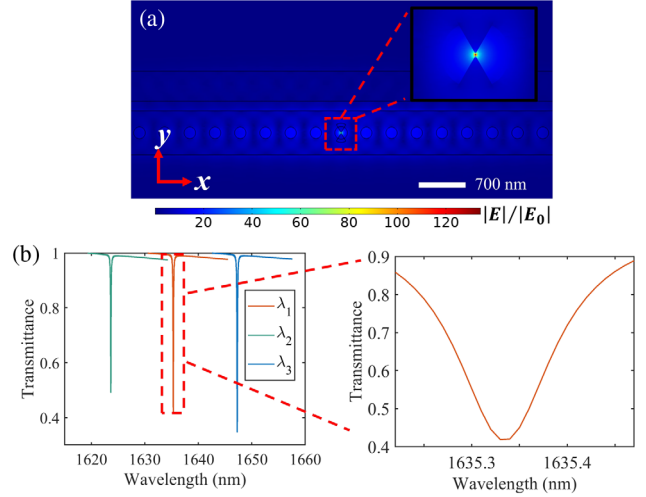

FIG. 2. (a) Electric field enhancement distribution of the BPCN cavity on resonance in the absence of the particle. The field enhancement is calculated by normalization to the amplitude of the electric field of the input fundamental TE mode in the bus waveguide. Inset: Zoom-in view of the bowtie region. (b) Transmission spectra for the three BPCNs, demonstrating the multiresonant property of the system. The resonant wavelengths are $\lambda_1 = 1635.33, \lambda_2 = 1623.65, \lambda_3 = 1647.28$ nm.

Here $\mathbf{E}\mathbf{E}^*$ and $\mathbf{H}\mathbf{H}^*$ are the outer products of the fields; I is the identity matrix; and ε and μ are the permittivity and the permeability of the medium surrounding the object, respectively. The effective transverse trapping potential resulting from the optical force is given by [49]

$$U(\mathbf{r}_0) = \int_\infty^{r_0} \mathbf{F}(\mathbf{r}) d\mathbf{r}. \tag{3}$$

Figure 3(a) illustrates the force spectra of a 10 nm diameter ($D = 10$ nm) PbSe quantum dot (refractive index $n = 4.73 + 0.24i$ [50]) positioned 21 nm above the center of the bowtie surface, showing a strong pulling force along the z direction (0.44 pN/2.5 mW). This trapping force is at least an order of magnitude higher than those achieved using Mie-resonant dielectric nanoantenna [51] and dielectric nanoantenna supporting anapole states [52]. Figures 3(b)–3(d) show the trapping potentials as well as the corresponding trapping forces when moving the quantum dot along the x, y and z directions, respectively. The depth of the trapping potential well is around 2 $k_B T$/2.5 mW for the x and y directions and 10 $k_B T$/2.5 mW for the z direction. Here k_B is the Boltzmann constant. This provides sufficient potential depth to stably confine the nanoparticle near the bowtie region.

Next, we explore the impact of the particle size and the vertical distance between the particle and the bowtie on the optical forces. We consider three different particle diameters ($D = 5$, 10, and 20 nm) for the quantum dot positioned at different distances (3, 9, 15, and 21 nm) from
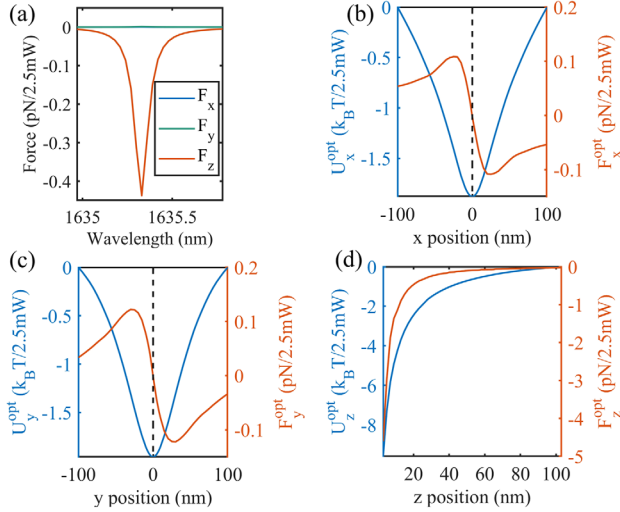
FIG. 3. Optical trapping characterization for a 10 nm PbSe quantum dot placed 21 nm above the bowtie surface. (a) Trapping force spectra for the quantum dot. (b)–(d) Trapping potential as well as trapping forces when moving the quantum dot along the x, y, and z directions, respectively. The vertical dashed lines in (b) and (c) denote the center of the bowtie.
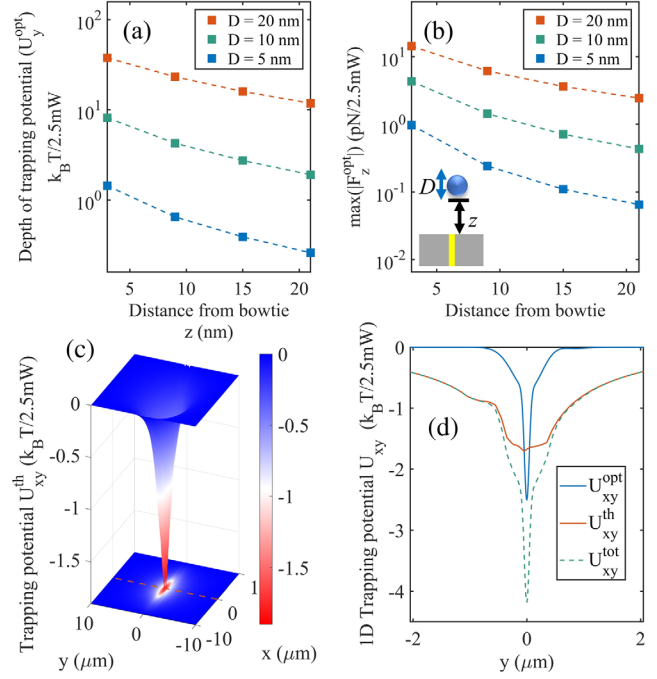

FIG. 4. (a) Depth of the trapping potential well along the y direction (U_y^{opt}) due to F_y^{opt} and (b) the maximum absolute value of the pulling force F_z^{opt} at different distances z from the bowtie surface [shown in the inset of (b)]. z is varied as 3, 9, 15, and 21 nm. Both y axes are in log scale. (c) Transverse thermophoretic trapping potential for a 10 nm quantum dot at $z = 21$ nm. (d) Transverse trapping potential for the optical trapping and thermophoretic trapping potentials along the y direction [red dash line in (c), $z = 21$ nm].

the bowtie surface. We choose these parameters for a comparison with a previously reported plasmonic nano-aperture [49]. Figure 4(a) shows the depth of the optical trapping potential well along the y direction (U_y^{opt}) with respect to F_y^{opt} and Fig. 4(b) shows the maximum absolute value of the pulling force F_z^{opt} as a function of the distance z measured from the quantum dot bottom to the bowtie surface (shown in the inset), respectively. Given the stable trapping requirement of 10 $k_B T$ for the trapping potential well, Fig. 4(a) indicates that the minimum power required for stable trapping of the three particles considered along the y direction is around 17, 3, and 0.7 mW, respectively, when z is 3 nm, which is less than a half of the power required by a plasmonic nanoaperture [49] taking into account the refractive index differences. Figure 4(b) shows that the maximum pulling force along the z direction is 0.97, 4.31, and 14.30 pN/2.5 mW for the three particles considered at the same distance ($z = 3$ nm). This pulling force drops exponentially as the particle moves away from the bowtie. Additional discussions on optical forces can be found in Supplemental Material S3 [16].

Optical power dissipated in the water layer near the bowtie establishes a thermal gradient. To calculate the temperature field distribution, the computed electric field distribution is used to determine the heat source density, which gives the heat dissipated per unit volume and is expressed as [53,54]

$$q(\mathbf{r}) = \frac{1}{2} \mathrm{Re}[\mathbf{J}_d^* (\mathbf{r}) \cdot \mathbf{E}(\mathbf{r})] = \frac{\omega}{2} \mathrm{Im}(\varepsilon) |\mathbf{E}(\mathbf{r})|^2, \quad (4)$$

where $\mathbf{J}_d = i\omega \mathbf{D}$ with $\mathbf{D} = \varepsilon \mathbf{E}$ is the displacement current density and ε is the permittivity of the specific material. Since water is the only lossy material in this system, the power density dissipated into water serves as the source term in the heat diffusion equation for computation of the temperature around the BPCN as well as in the surrounding fluid and substrate. The temperature field in the system is determined by solving the steady-state heat equation given by

$$\nabla \cdot [-\kappa \nabla T(\mathbf{r}) + \rho c_p T(\mathbf{r})\mathbf{u}(\mathbf{r})] = q(\mathbf{r}). \quad (5)$$

The first term on the left is the heat conduction term, while the second term is the convection term, which depends on the velocity of the fluid. $T(\mathbf{r})$ and $\mathbf{u}(\mathbf{r})$ are spatial temperature and fluid velocity field, respectively, and the material properties κ, ρ and c_p are thermal conductivity, density and specific heat capacity, respectively.

Thermophoresis phenomenon [17,55] is the motion of particles or molecules in the presence of thermal gradients and provides an attractive trapping force under negative thermophoresis [18,19,56]. Details of the calculation of the negative thermophoretic force are provided in the

Supplemental Material S4 [16]. To compare with the optical trapping, Figure 4(c) illustrates the simulated transverse thermophoretic trapping potential (U_{xy}^{th}) for 10 nm particle at $z = 21$ nm. The thermophoretic trapping potential has the same order of magnitude as the optical trapping potential shown in Figure 3, whereas the thermophoretic trapping potential well is much broader than the optical one. For emphasis, the transverse optical trapping and thermophoretic trapping potentials along the y axis are shown in Figure 4(d). The asymmetry of the thermophoretic trapping potential curve results from the bus waveguide which affects the heat diffusion. The superposition of the optical trapping and the thermophoretic trapping achieves a long range and 1.7 times deeper trapping potential well. In our system, the force that prevents particles from getting too close or stuck to the surface of the BPCN comes from the interaction between charged surfaces (surface of the particle and the BPCN) in liquid media, described by the DLVO theory [20]. Detailed discussions can be found in Supplemental Material S9 [16].

Next, we demonstrate the long-range and rapid transport of individual nanoparticles to the vicinity of the bowtie for optical trapping by generating wavelength-dependent electrohydrodynamic microfluidic vortices based on the electrothermal flow effect in a microfluidic channel. The thermal gradient induced in the water layer near the bowtie results in a gradient in the permittivity and electrical conductivity of the water medium near the bowtie. An applied ac electric field acts on these gradients to create a volumetric body force in the fluid due to the electrothermal effect [57,58].

By leveraging the configuration of the cascaded BPCNs, the body force of the electrothermal flow in our system is not only space dependent, but also *wavelength dependent*. That means the spatial distribution of the local temperature gradient can additionally be controlled by the wavelength of the input light, as shown in Fig. 5(d). Following a perturbative expansion [57], the wavelength dependent time-averaged electrothermal body force per unit volume at ac frequency ω can be expressed as

$$\langle F_{ET} \rangle \hat{z} = \frac{1}{2} \varepsilon E_z^2 \left[\frac{\sigma^2 \varepsilon (\alpha - \gamma)}{\sigma^2 + \omega^2 \varepsilon^2} - \frac{1}{2} \alpha \right] \frac{\partial T(z, \lambda)}{\partial z} \hat{z}, \quad (6)$$

$$\langle F_{ET} \rangle \hat{r} = -\frac{1}{4} \varepsilon \alpha E_z^2 \frac{\partial T(r, \lambda)}{\partial r} \hat{r}, \quad (7)$$

where $\lambda = \lambda_1, \lambda_2, \lambda_3 \ldots \lambda_n$ and n is the number of the cascaded BPCNs; ε, $\tau = \varepsilon/\sigma$, σ and ω are the fluid permittivity, charge relaxation time, electrical conductivity, and applied ac frequency, respectively; α and γ are expressed as $\alpha = (1/\varepsilon)(\partial \varepsilon/\partial T)$, $\gamma = (1/\sigma)(\partial \sigma/\partial T)$ and are given as -0.004 and 0.02 K^{-1}, respectively [59]. Equations (6) and (7) describe the axial and radial components of the electrothermal body force.

The velocity field distribution of the fluidic flow when a given BPCN is excited is determined from the solution of the incompressible Navier-Stokes equations given by

$$\rho_0(\mathbf{u}(\mathbf{r}) \cdot \nabla)\mathbf{u}(\mathbf{r}) + \nabla p(\mathbf{r}) - \eta \nabla^2 \mathbf{u}(\mathbf{r}) = \mathbf{F}, \quad (8)$$

$$\nabla \cdot \mathbf{u} = 0. \quad (9)$$

The forcing term $\mathbf{F}$ in Eq. (8) describes the body force per unit volume acting on the fluid element, which is given by Eqs. (6) and (7). We note that the contribution from the buoyancy-driven convection is negligible in this system (see Supplemental Material S7 [16] for details).

Figure 5(a) shows the temperature field distribution in the xy plane 300 nm above the bowtie surface. A temperature rise of 10.6 K is observed and the superimposed
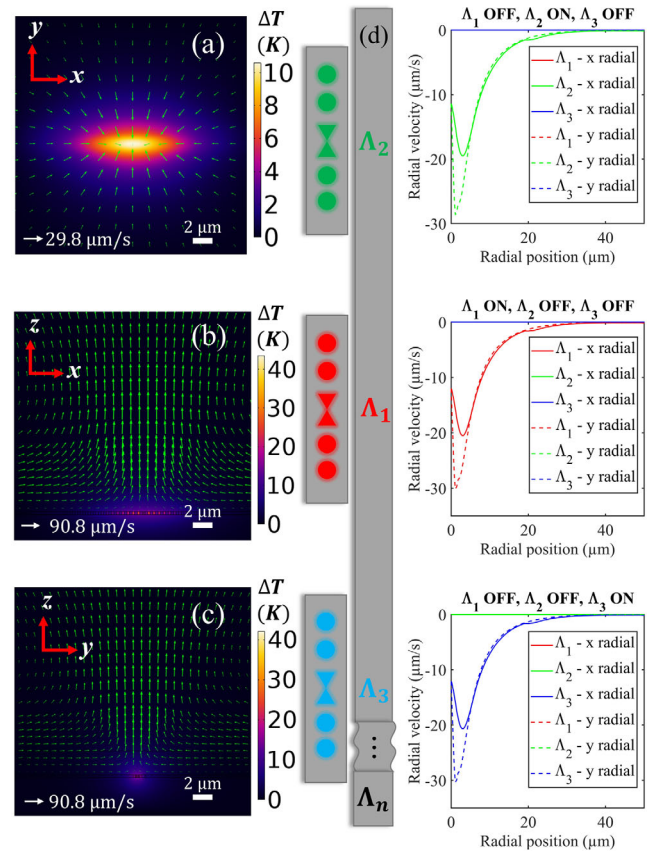
FIG. 5. (a) Temperature field distribution of the xy plane 300 nm above the bowtie surface. The radial velocity vector plot of the electrothermal flow induced around the resonant BPCN is superimposed on the temperature profile. Arrow length represents the magnitude of the flow velocity. (b) Temperature field distribution of the xz plane and (c) the yz plane. (d) Illustration of three cascaded BPCNs placed beside a bus waveguide. The right three panels show corresponding radial velocity profiles of the induced electrothermal flow along x and y directions (300 nm above the bowtie surface) around the three BPCNs in different states. The electrothermal flow shows a long-range characteristic ($\sim$50 μm); (a) to (c) corresponds to the Λ_1 panel.

radial velocity vector plot of the flow shows that the induced electrothermal flow is directed radially inwards towards the thermal hotspot generated by water around the bowtie and serves as a powerful means to deliver suspended particles to the bowtie region. The maximum radial flow velocity is about 29.8 μm/s, which is directed to the bowtie and hence much more efficient than traditional particle delivery methods such as pressure-driven flow and slow Brownian motion. Furthermore, this flow velocity is at least 20 times greater than the 1 μm/s thermoplasmonic convection flow velocity achievable with an array of optimized plasmonic bowtie nanoantenna [60]. Figures 5(b) and 5(c) show the temperature profile in the xz and the yz plane. The maximum temperature rise is 43.6 K under only 2.5 mW input power due to the high field enhancement. The superimposed velocity vectors verify the induced electrothermal vortex flow shown in Fig. 1. We note here that the maximum Stokes drag force along the z direction exerted on the particles (10 nm quantum dot for example) from the electrothermal flow is estimated to be far below the order of magnitude of the optical gradient force shown in Fig. 3(a) (e.g., 0.0076 pN drag force for the 10 nm quantum dot). Therefore, the electrothermal flow mainly assists in transporting the particles to the vicinity of the BPCN.

Figure 5(d) demonstrates the concept of multiplexed nanoparticle transport and nano-optical trapping with the cascaded BPCNs shown in Fig. 1. When the input wavelength is tuned to λ_1, only the middle BPCN (Λ_1) with a resonance wavelength of λ_1 is excited while the other two are off resonance and not excited. Therefore, the electrothermal flow is only induced around Λ_1 (see the radial velocity plot in the middle panel). By integrating over the radial velocity curve when Λ_2 is on, we estimate that it takes about 8 seconds for the flow to transport a nanoparticle 25 μm from the vicinity of Λ_1 to Λ_2. The high Q characteristic of the bowtie PhC permits to integrate multiple BPCNs along the low-loss bus waveguide to provide the means to achieve long range particle hand-off from tens of microns to millimeter scale distances by simply switching the wavelength of the input light. We note that the electrothermal flow along the y direction shows a larger magnitude of velocity in comparison to the electrothermal flow along the x direction. This is attributed to the asymmetric spatial distribution of the in-plane thermal hotspots. It is evident that there is a higher temperature gradient along the y direction and hence a stronger electrothermal flow velocity in comparison to that along the x direction. The slightly different radial velocity values presented in the three panels are attributed to the different electric field enhancements of the three BPCNs.

We have proposed and systematically studied a cascaded bowtie photonic crystal nanobeam system that can achieve multiplexed long-range electrohydrodynamic transport and optical trapping of nanoscale particles. Compared with traditional 1D photonic crystal nanobeams, our bowtie photonic crystal cavity can more strongly confine and enhance the electromagnetic field while maintaining a high quality factor. The extremely localized field provides a strong field gradient that is ideal for trapping sub-20 nm particles. Furthermore, the localized water absorption near the cavities serves as heat sources to generate negative thermophoresis that can assist in the optical trapping process. Finally, we harness the localized water absorption to induce on-demand electrothermal flow that can efficiently transport nanoparticles to the vicinity of the localized field of the bowtie photonic crystal cavity region for enhanced optical trapping. Our proposed multiplexed platform could enable millimeter scale transport and hand-off of particles across cavities in miniaturized optofluidic chips by simply switching the wavelength. We envision that our system will be a promising platform in many fields of biology and quantum information, such as in single molecule characterization and assembly of single photon sources.

J. C. N. and S. M. W. conceived and guided the project. J. A. A designed the photonic crystal cavity. S. Y. and J. A. A. performed the wave-optics simulations in Lumerical. S. Y. implemented the photonic crystal design in COMSOL and performed the wave-optics and Multiphysics simulations in COMSOL. C. H. contributed to the Multiphysics simulations and K. P. A. contributed to the Lumerical simulations. J. A. A. wrote the bowtie PhC design section (S1 of the Supplemental Material [16]) and S. Y. wrote the manuscript and the rest of Ref. [16]. J. C. N. and S. M. W. contributed to editing the manuscript.

[*]These authors contribute equally to this work.
[†]justus.ndukaife@vanderbilt.edu

[1] Q. Hu, D. H. Xu, Y. Zhou, R. W. Peng, R. H. Fan, N. X. Fang, Q. J. Wang, X. R. Huang, and M. Wang, Position-sensitive spectral splitting with a plasmonic nanowire on silicon chip, Sci. Rep. **3**, 3095 (2013).

[2] J. A. Schuller, E. S. Barnard, W. Cai, Y. C. Jun, J. S. White, and M. L. Brongersma, Plasmonics for extreme light concentration and manipulation, Nat. Mater. **9**, 193 (2010).

[3] Y. Zhu, H. Jing, R. W. Peng, C. Y. Li, J. He, B. Xiong, and M. Wang, Realizing anderson localization of surface plasmon polaritons and enhancing their interactions with excitons in 2d disordered nanostructures, Appl. Phys. Lett. **116**, 201106 (2020).

[4] X. Xiong, S. Wei, W. Tang, R. Peng, R. Peng, M. Wang, M. Wang, and M. Wang, Realizing transmissive and reflective focusing with an on-chip metalens, Opt. Lett. **47**, 3696 (2022).

[5] H. Altug, S. H. Oh, S. A. Maier, and J. Homola, Advances and applications of nanophotonic biosensors, Nat. Nanotechnol. **17,** 5 (2022).

[6] J. Berthelot, S. S. Aćimović, M. L. Juan, M. P. Kreuzer, J. Renger, and R. Quidant, Three-dimensional manipulation with scanning near-field optical nanotweezers, Nat. Nanotechnol. **9,** 295 (2014).

[7] C. Hong, S. Yang, I. I. Kravchenko, and J. C. Ndukaife, Electrothermoplasmonic trapping and dynamic manipulation of single colloidal nanodiamond, Nano Lett. **21,** 4921 (2021).

[8] M. Geiselmann, R. Marty, J. Renger, F. J. G. D. Abajo, and R. Quidant, Deterministic optical-near-field-assisted positioning of nitrogen-vacancy centers, Nano Lett. **14,** 1520 (2014).

[9] J. D. Joannopoulos, S. G. Johnson, J. N. Winn, and R. D. Meade, *Photonic Crystals: Molding the Flow of Light (Second Edition)* (Princeton University Press, Princeton, NJ, 2011).

[10] S. Hu, M. Khater, R. Salas-Montiel, E. Kratschmer, S. Engelmann, W. M. Green, and S. M. Weiss, Experimental realization of deep-subwavelength confinement in dielectric optical resonators, Sci. Adv. **4,** eaat2355 (2018).

[11] Y. F. Chen, X. Serey, R. Sarkar, P. Chen, and D. Erickson, Controlled photonic manipulation of proteins and other nanomaterials, Nano Lett. **12,** 1633 (2012).

[12] X. Serey, S. Mandal, Y. F. Chen, and D. Erickson, DNA Transport and Delivery in Thermal Gradients Near Optofluidic Resonators, Phys. Rev. Lett. **108,** 1 (2012).

[13] Y. Gao and Y. Shi, Design of a single nanoparticle trapping device based on bow-tie-shaped photonic crystal nanobeam cavities, IEEE Photonics J. **11** (2019).

[14] J. C. Ndukaife, A. V. Kildishev, A. G. A. Nnanna, V. M. Shalaev, S. T. Wereley, and A. Boltasseva, Long-range and rapid transport of individual nano-objects by a hybrid electrothermoplasmonic nanotweezer, Nat. Nanotechnol. **11,** 53 (2016).

[15] F. O. Afzal, S. I. Halimi, and S. M. Weiss, Efficient side-coupling to photonic crystal nanobeam cavities via state-space overlap, J. Opt. Soc. Am. B **36,** 585 (2019).

[16] See Supplemental Material at http://link.aps.org/supplemental/10.1103/PhysRevLett.130.083802 for descriptions of the optimization process for the photonic crystals, details of the numerical simulations, additional discussions on the optical gradient and thermophoretic forces, discussions on dlvo potential, and experiment designs, which includes Refs. [10,12,14,15,17–47].

[17] R. Piazza and A. Parola, Thermophoresis in colloidal suspensions, J. Phys. Condens. Matter **20** (2008).

[18] L. Lin, X. Peng, X. Wei, Z. Mao, C. Xie, and Y. Zheng, Thermophoretic tweezers for low-power and versatile manipulation of biological cells, ACS Nano **11,** 3147 (2017).

[19] L. Lin, X. Peng, Z. Mao, X. Wei, C. Xie, and Y. Zheng, Interfacial-entropy-driven thermophoretic tweezers, Lab Chip **17,** 3061 (2017).

[20] M. Fränzl and F. Cichos, Hydrodynamic manipulation of nano-objects by optically induced thermo-osmotic flows, Nat. Commun. **13** (2022).

[21] S. Hu and S. M. Weiss, Design of photonic crystal cavities for extreme light concentration, ACS Photonics **3,** 1647 (2016).

[22] S. I. Halimi, Z. Fu, F. O. Afzal, J. A. Allen, S. Hu, and S. M. Weiss, Controlling the mode profile of photonic crystal nanobeam cavities with mix-and-match unit cells, J. Opt. Soc. Am. B **37,** 3401 (2020).

[23] S. Kim, H.-M. Kim, and Y.-H. Lee, Single nanobeam optical sensor with a high q-factor and high sensitivity, Opt. Lett. **40,** 5351 (2015).

[24] J. Barzilai and J. M. Borwein, Two-point step size gradient methods, IMA J. Numer. Anal. **8,** 141 (1988).

[25] S. I. Halimi, Z. Fu, F. O. Afzal, J. A. Allen, S. Hu, and S. M. Weiss, Photonic crystal design with mix and match unit cells for mode manipulation, in *CLEO: Science and Innovations* (Optical Society of America, 2019), pp. SM2J–4, 10.1364/CLEO_SI.2019.SM2J.4.

[26] Z. Dong, S. Gorelik, R. Paniagua-Dominguez, J. Yik, J. Ho, F. Tjiptoharsono, E. Lassalle, S. D. Rezaei, D. C. Neo, P. Bai *et al.*, Silicon nanoantenna mix arrays for a trifecta of quantum emitter enhancements, Nano Lett. **21,** 4853 (2021).

[27] R. Regmi, J. Berthelot, P. M. Winkler, M. Mivelle, J. Proust, F. Bedu, I. Ozerov, T. Begou, J. Lumeau, H. Rigneault *et al.*, All-dielectric silicon nanogap antennas to enhance the fluorescence of single molecules, Nano Lett. **16,** 5143 (2016).

[28] M. Caldarola, P. Albella, E. Cortés, M. Rahmani, T. Roschuk, G. Grinblat, R. F. Oulton, A. V. Bragas, and S. A. Maier, Non-plasmonic nanoantennas for surface enhanced spectroscopies with ultra-low heat conversion, Nat. Commun. **6,** 1 (2015).

[29] C. Hong, S. Yang, and J. C. Ndukaife, Stand-off trapping and manipulation of sub-10 nm objects and biomolecules using opto-thermo-electrohydrodynamic tweezers, Nat. Nanotechnol. **15,** 908 (2020).

[30] K. Wang and K. B. Crozier, Plasmonic trapping with a gold nanopillar, ChemPhysChem **13,** 2639 (2012).

[31] T. Zhu, Y. Cao, L. Wang, Z. Nie, T. Cao, F. Sun, Z. Jiang, M. Nieto-Vesperinas, Y. Liu, C.-W. Qiu *et al.*, Self-Induced Backaction Optical Pulling Force, Phys. Rev. Lett. **120,** 123901 (2018).

[32] K. C. Neuman and S. M. Block, Optical trapping, Rev. Sci. Instrum. **75,** 2787 (2004).

[33] J. Burelbach, M. Zupkauskas, R. Lamboll, Y. Lan, and E. Eiser, Colloidal motion under the action of a thermophoretic force, J. Chem. Phys. **147,** 094906 (2017).

[34] S. A. Putnam, D. G. Cahill, and G. C. Wong, Temperature dependence of thermodiffusion in aqueous suspensions of charged nanoparticles, Langmuir **23,** 9221 (2007).

[35] A. Würger, Hydrodynamic Boundary Effects on Thermophoresis of Confined Colloids, Phys. Rev. Lett. **116,** 1 (2016).

[36] B. V. Derjaguin, N. V. Churaev, and V. M. Muller, *Surface Forces* (Springer, New York, 1987).

[37] L. Lin, M. Wang, X. Peng, E. N. Lissek, Z. Mao, L. Scarabelli, E. Adkins, S. Coskun, H. E. Unalan, B. A. Korgel, L. M. Liz-Marzán, E. L. Florin, and Y. Zheng, Opto-thermoelectric nanotweezers, Nat. Photonics **12,** 195 (2018).

[38] L. Lin, J. Zhang, X. Peng, Z. Wu, A. C. Coughlan, Z. Mao, M. A. Bevan, and Y. Zheng, Opto-thermophoretic assembly of colloidal matter, Sci. Adv. **3**, e1700458 (2017).

[39] Q. Jiang, B. Rogez, J.-B. Claude, G. Baffou, and J. Wenger, Quantifying the role of the surfactant and the thermophoretic force in plasmonic nano-optical trapping, Nano Lett. **20**, 8811 (2020).

[40] D. Yang, C. Lu, H. Yin, and I. P. Herman, Thermoelectric performance of pbse quantum dot films, Nanoscale **5**, 7290 (2013).

[41] G. S. Shanker, A. Swarnkar, A. Chatterjee, S. Chakraborty, M. Phukan, N. Parveen, K. Biswas, and A. Nag, Electronic grade and flexible semiconductor film employing oriented attachment of colloidal ligand-free pbs and pbse nanocrystals at room temperature, Nanoscale **7**, 9204 (2015).

[42] S. Yang, C. Hong, Y. Jiang, and J. C. Ndukaife, Nanoparticle trapping in a quasi-bic system, ACS Photonics **8**, 1961 (2021).

[43] J. N. Israelachvili, *Intermolecular and Surface Forces* (Academic Press, New York, 2011).

[44] H. C. Hamaker, The London–van der Waals attraction between spherical particles, Physica (Amsterdam) **4**, 1058 (1937).

[45] G. Chen, Z. Ni, Y. Bai, Q. Li, and Y. Zhao, The role of interactions between abrasive particles and the substrate surface in chemical-mechanical planarization of si-face 6h-sic, RSC Adv. **7**, 16938 (2017).

[46] E. Rabani, An interatomic pair potential for cadmium selenide, J. Chem. Phys. **116**, 258 (2002).

[47] K. Hu and A. J. Bard, Characterization of adsorption of sodium dodecyl sulfate on charge-regulated substrates by atomic force microscopy force measurements, Langmuir **13**, 5418 (1997).

[48] M. Ploschner, Optical forces near a nanoantenna, J. Nanophoton. **4**, 041570 (2010).

[49] A. A. Saleh and J. A. Dionne, Toward efficient optical trapping of sub-10-nm particles with coaxial plasmonic apertures, Nano Lett. **12**, 5581 (2012).

[50] Z. Hens and I. Moreels, Light absorption by colloidal semiconductor quantum dots, J. Mater. Chem. **22**, 10406 (2012).

[51] Z. Xu, W. Song, and K. B. Crozier, Optical trapping of nanoparticles using all-silicon nanoantennas, ACS Photonics **5**, 4993 (2018).

[52] J. J. Hernández-Sarria, O. N. Oliveira, and J. R. Mejía-Salazar, Toward Lossless Infrared Optical Trapping of Small Nanoparticles Using Nonradiative Anapole Modes, Phys. Rev. Lett. **127**, 186803 (2021).

[53] G. Baffou and R. Quidant, Thermo-plasmonics: Using metallic nanostructures as nano-sources of heat, Laser Photonics Rev. **7**, 171 (2013).

[54] G. Baffou, C. Girard, and R. Quidant, Mapping Heat Origin in Plasmonic Structures, Phys. Rev. Lett. **104** (2010).

[55] R. Piazza, 'Thermal forces': colloids in temperature gradients, J. Phys. Condens. Matter **16**, S4195 (2004).

[56] Y. Lamhot, A. Barak, O. Peleg, and M. Segev, Self-Trapping of Optical Beams Through Thermophoresis, Phys. Rev. Lett. **105**, 1 (2010).

[57] A. Ramos, H. Morgan, N. G. Green, and A. Castellanos, Ac electrokinetics: A review of forces in microelectrode structures, J. Phys. D **31**, 2338 (1998).

[58] J. R. Melcher and M. S. Firebaugh, Traveling wave bulk electroconvection induced across a temperature gradient, Phys. Fluids **10**, 1178 (1967).

[59] D. R. Lide, *CRC Handbook of Chemistry and Physics*, 84th edition, (CRC Press, 2003), Vol. 85.

[60] B. J. Roxworthy, A. M. Bhuiya, S. P. Vanka, and K. C. Toussaint, Understanding and controlling plasmon-induced convection, Nat. Commun. **5**, 1 (2014).